

Template for preparing your research report submission to PNAS using Overleaf

Author One^{a,c,1}, Author Two^{b,1,2}, and Author Three^a

^aAffiliation One; ^bAffiliation Two; ^cAffiliation Three

This manuscript was compiled on August 16, 2017

We present a conceptual and computational framework to unify today's theories of neuromuscular control called feasibility theory. We begin by describing how the musculoskeletal anatomy of the limb, the need to control individual tendons, and the physics of a motor task uniquely specify the family of all valid muscle activations that accomplish it (its 'feasible activation space'). For our example of static force production with a finger with seven muscles, computational geometry characterizes, in a complete way, the structure of feasible activation spaces as 3-dimensional polytopes embedded in 7-D. The feasible activation space for a given task is the landscape where all neuromuscular learning, control, and performance must occur. This approach unifies current theories of neuromuscular control because the structure of feasible activation spaces can be separately approximated as either low-dimensional basis functions (synergies), high-dimensional joint probability distributions (Bayesian priors), or fitness landscapes (to optimize cost functions).

Neuromechanics | Motor Control | Tendon actuation | ...

This PNAS journal template is provided to help you write your work in the correct journal format. Instructions for use are provided below.

Note: Please start your introduction without including the word "Introduction" as a section heading (except for math articles in the Physical Sciences section); this heading is implied in the first paragraphs.

Introduction

How the nervous system selects specific levels of muscle activations (i.e. a muscle activation pattern) for a given motor task continues to be hotly debated. Some suggest the nervous system either combines low-dimensional synergies (? ? ? ? ?), learns probabilistic representations of valid muscle activation patterns (? ? ? ?), or optimizes physiologically-tenable cost functions (? ? ? ? ? ?). At the core of this problem lies the nature of 'feasible activation spaces,' and the computational challenge of describing and understanding their high-dimensional structure (for an overview, see (?)). A feasible activation space is the family of valid solutions (i.e. muscle activation patterns) available to the nervous system to produce a given motor task. Fig. 1 illustrates the neuromechanical interactions that define the feasible activation space for a particular task.

The most the nervous system can do, therefore, is select a specific muscle activation pattern from within the feasible activation space—as muscle activation patterns outside of this space are, by definition, inappropriate for the task. In fact, the feasible activation space defines the landscape upon which all neuromuscular learning and performance must occur. Understanding neuromuscular control is, therefore, equivalent to understanding how the nervous system finds, explores, inhab-

its, and exploits the structure of feasible activation spaces (? ? ? ? ? ? ?).

But the 'curse of dimensionality' (? ? ?) makes it computationally challenging to calculate, describe, and understand the nature and structure of high-dimensional feasible activation spaces (? ? ? ? ? ? ?)—even for an isolated human finger or cat leg generating everyday static forces (? ? ? ?). This is due to the computational complexity of algorithms applied upon high dimensional spaces.

Current theories of neuromuscular control are alternative responses to the curse of dimensionality, which at times can be seen as competing, rather than complementary. However, the fundamental neuromechanics of the limb and the physics of the task are the common ground for all theories. Thus, understanding the nature and structure of feasible activation spaces would help compare, contrast and combine these alternative approaches to neuromuscular control.

We now propose a conceptual and computational framework to provide complete characterizations of feasible activation spaces, thereby contextualizing and unifying multiple theories of neuromuscular control. As an example, we leverage prior work (? ? ?) to now describe the structure of the feasible activation space for the seven muscles of the index finger when producing static fingertip force. This is the type of fingertip force observed when, for example, pressing hard on a table without finger movement, and is also referred to as an isometric force task. In this case, the feasible activation space is a polytope embedded in 7-dimensional muscle activation space. A polytope is the name given to bounded convex polyhedra in dimensions higher than 3. Our computational approach hinges on the efficient sampling and complete representation of the structure of high-dimensional polytopes. This then character-

Significance Statement

Wings take flight, eyes refract light, and muscles manipulate bones within the interplaying constraints of Newtonian physics. Here we apply the basic tenets of physics to the field of neuromechanical control, to elucidate the neuro-physical-motor landscape upon which evolution and learning operate. With three interweaving hypotheses of motor control in the literature, we fill the gap between the disparate approaches by recontextualizing the problem of force control as a physical constraints problem, thereby lighting the stage of optimal, synergistic, and bayesian control.

Please provide details of author contributions here.

Please declare any conflict of interest here.

¹A.O.(Author One) and A.T. (Author Two) contributed equally to this work (remove if not applicable).

²To whom correspondence should be addressed. E-mail: author.two@email.com

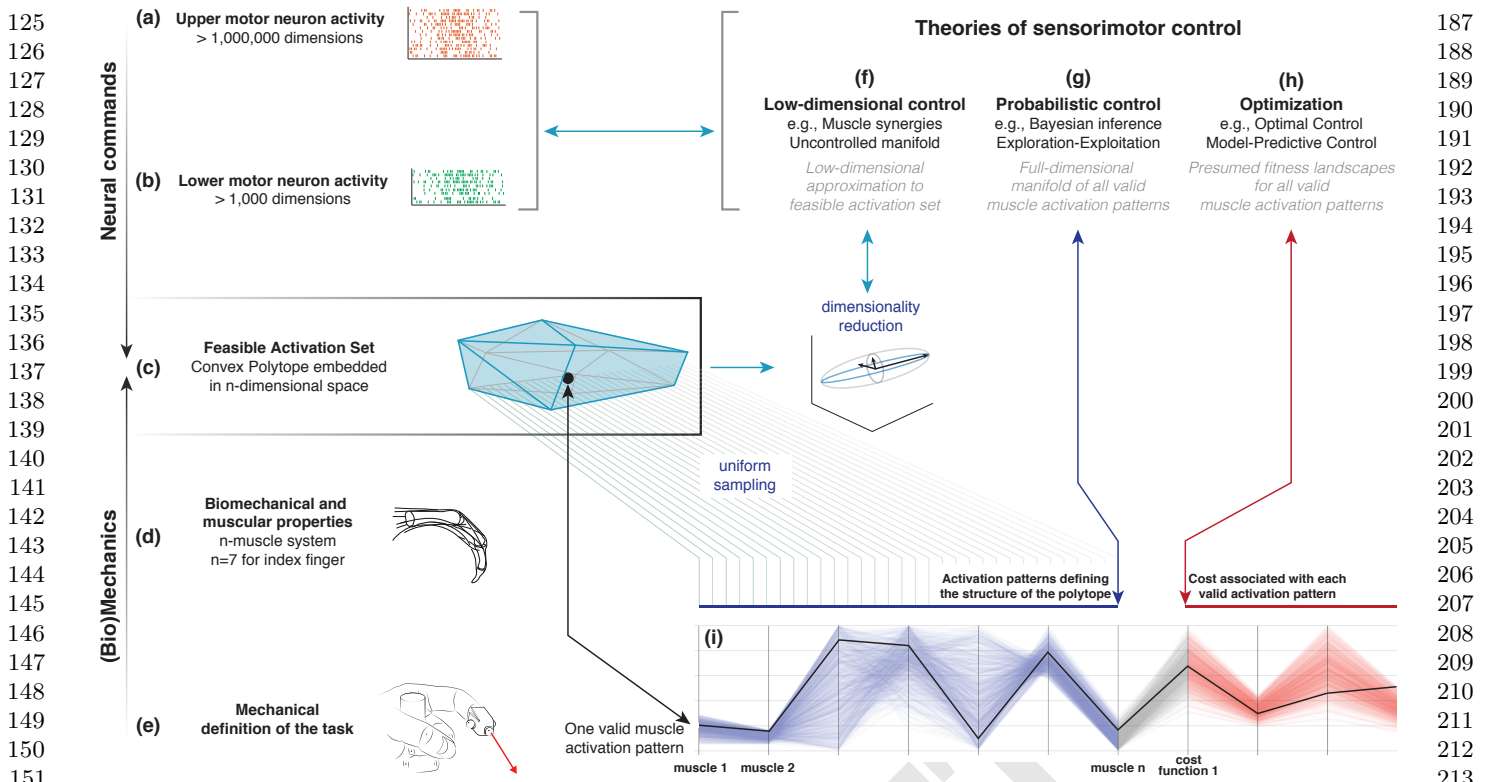


Fig. 1. Feasible activation spaces guiding sensorimotor control of a task. The descending motor command for a given task is issued by the primary motor cortex (a), which projects onto alpha-motor neuron pools in the spinal cord (b). The combined drive to all alpha-motor neurons of a muscle can be considered its total muscle activation level (a value between 0 and 1). If we consider that motor commands are sent to multiple independently controlled muscles, then the overall motor command can be conceptualized as a multi-dimensional muscle activation pattern (i.e., a point) in a high-dimensional muscle activation space (?? ? ? ?) (c). For that muscle activation pattern to be valid, it has to elicit muscle forces (d) capable of satisfying the mechanical requirements of the task—in this case a well directed fingertip force (e). Given the large number of muscles in vertebrates, there is muscle redundancy; there is a large number of valid muscle activation patterns that can produce a given task. We propose that our novel ability to characterize the high-dimensional structure of feasible activation spaces (i) allows us to compare, contrast and reconcile today's three dominant approaches to redundancy in sensorimotor control (f, g, h).

159
160
161
162
163
164
165
166
167
168
169
170
171
172
173
174
175
176
177
178
179
180
181
182
183
184
185
186
izes all valid muscle activation patterns. These computational techniques can scale up to ~40 dimensions, which suffices to analyze the neural control of all muscles in an extant vertebrate limb systems. By providing a complete characterization of all muscle activation patterns for a given motor task, we are able to compare, contrast, combine—and reconcile—today's three dominant approaches to neuromuscular control.

Results

The goal of this work is to use different perspectives to describe the high-dimensional structure of these feasible activation spaces; we then show how these spaces allow us to unify today's theories of neuromuscular control. We used our realistic index finger model to calculate the feasible activation space for the task of producing static fingertip force in the distal direction (see Fig. 1). The model represents each muscle's contribution to fingertip force as a directed force vector at the fingertip; there are 7 of these force vectors at the index fingertip. As described briefly in the Methods, Hit-and-Run is a method in polytope sampling that we use to sample from the infinite number of muscle activations within the feasible activation space. In effect, given a fingertip task force and the maximum linear fingertip forces each muscle creates, we can collect the muscle activations required to produce that task. As we can now collect thousands of muscle activation patterns for any

isometric force task, we examined how the feasible activation spaces (and their representations) change with increasing task intensity in the distal direction (Fig. 1e).

We collected points for multiple task intensities between 0% (i.e., pure co-contraction without output force) and 100% of maximal static force.

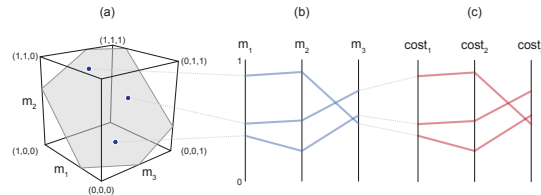


Fig. 2. Characterizing the high-dimensional structure of a feasible activation space via parallel coordinates. Consider three points (i.e., muscle activation patterns in Supplemental Fig. 8e) from the feasible activation space (a). The activation level for each muscle (i.e., the coordinates of each point) are sewn across three vertical parallel axes (b). As is common when evaluating multiple valid coordination patterns, each point can be assigned a cost as per an assumed cost function. The associated cost for each muscle activation pattern can also be shown as an additional dimension. We show three representative cost functions (c). Activation levels are bound between 0 and 1, and costs are normalized to their respective observed ranges.

249
250
251
252
253
254
255
256
257
258
259
260
261
262
263
264
265
266
267
268
269
270
271
272
273
274
275
276
277
278
279
280
281
282
283
284
285
286
287
288
289
290
291
292
293
294
295
296
297
298
299
300
301
302
303
304
305
306
307
308
309
310

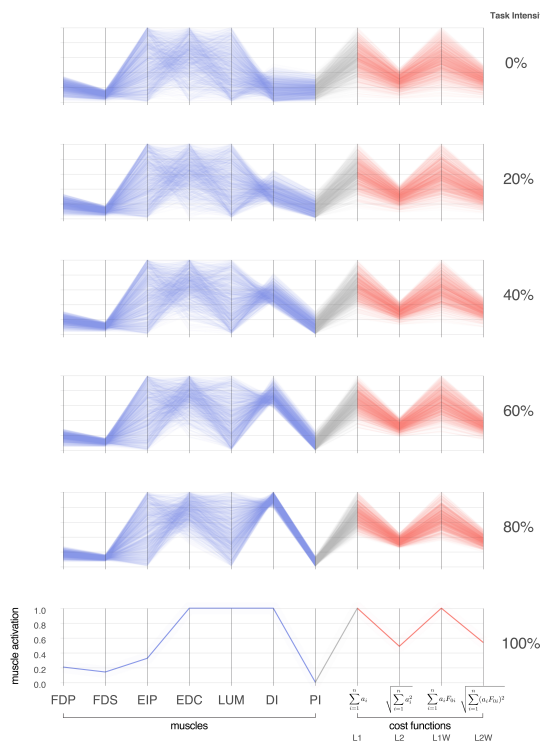


Fig. 3. Activation patterns of the seven muscles of the index finger across six magnitudes of a fingertip force The connectivity across parallel coordinates shows how muscle activation patterns are related in multiple ways to produce a fingertip force vector between 0 (a) to 100% (f) of maximal magnitude. At these extremes we have, respectively, the coordination patterns that produce pure co-contraction and the one unique solution for maximal output. In between, we see the how the structure of the feasible activation spaces changes as redundancy is lost. In blue are the activation values, and in red are normalized costs for four cost functions common in the literature. *FDP*: flexor digitorum profundus, *FDS*: flexor digitorum superficialis, *EIP*: extensor indicis proprius, *EDC*: extensor digitorum communis, *LUM*: lumbrical, *DI*: dorsal interosseous, *PI*: palmar interosseous.

Parallel coordinate visualization naturally reveals the structure of the feasible activation space. We used Hit-and-Run to sample from feasible activation spaces for 6 task intensities, labeled as task intensities α of 0.0, 0.2, 0.4, 0.6, 0.8 and 1.0. For each task intensity, we ran 100,000 Hit-and-Run iterations and down-sampled to every 100th point to produce 1,000 points that are (in our experiments) uncorrelated and uniformly distributed in P . Recall that approaching 100% of maximal force shrinks P to a single, unique solution (?).

Parallel coordinate visualization effectively reveals correlations that exist among the 1,000 valid muscle activation patterns for each magnitude of desired fingertip force, and activation pattern cost, Fig. 2 and Fig. 3.

An interactive parallel coordinate visualization plot can be accessed at <https://briancohn.github.io/space-parcoords/>. This interactive interface for parallel coordinate visualization allows us to explore subsets of the valid muscle activation patterns.

For example, restricting the range of muscle activation of one or more muscles shows us the necessary activation levels of the remaining muscles. This can be used to, say, simulate a 40% reduction in possible activation to some muscles (e.g., due to a peripheral neuropathy) in the extrinsic extensor muscles of the index finger innervated by the radial nerve (EIP and EDC) (?).

Figures in the Supplemental Material show how, for 80% of task intensity (i.e., 80% of maximal force output), only 29% (i.e., $\frac{290}{1,000}$) of all possible solutions survive when capping the maximal excitation of EIP and EDC at 60%. Thus, any neural or muscle dysfunction that compromises the ability of the extensor muscles will limit the choices the nervous system has to produce this force—even at sub-maximal levels. These results further challenge the notion of muscle redundancy as discussed in detail in (? ?).

Moreover, this same case of task intensity of 80% and maximal excitation of EIP $\leq 60\%$ reveals important and counterintuitive consequences in the control of musculature. For example, the range of feasible activation level for some muscles do not change too much (FDP, FDS, and LUM), but does change for others (DI and PI). Most interestingly, the range of costs across valid solutions remains broad.

Similarly, we can describe any subset of muscle activation patterns associated with specific ranges for a given cost function. Figures in the Supplemental Material also show how can characterize all muscle activation patterns associated with the lowest 10% of L2 weighted costs. The coordination patterns that meet this strict criterion are quite different from one another (note the broad ranges and criss-cross patterns).

These relationships among all valid 7-dimensional muscle activations patterns reveal important aspects of the structure of the feasible activation space, and its associated cost landscapes. We see one muscle can affect other muscles in different ways: while limiting PI to 20% of maximal activation eliminates 30.1% of the valid solutions, limiting DI to 20% eliminates 42.8% of them. Similarly we can distinguish between changes in the extreme values of muscle activation from changes in the number of valid solutions. Consider the range of activation for DI and PI at task intensity of 80% which lies between 0 and 0.52 and 0.39, respectively. Limiting DI to 20% pulls PI's maximum down by nearly 0.20, and the converse

311
312
313
314
315
316
317
318
319
320
321
322
323
324
325
326
327
328
329
330
331
332
333
334
335
336
337
338
339
340
341
342
343
344
345
346
347
348
349
350
351
352
353
354
355
356
357
358
359
360
361
362
363
364
365
366
367
368
369
370
371
372

373 has nearly the same effect. However, in both cases, the median
 374 activation among surviving solutions changes no more than
 375 0.06. This emphasizes that understanding feasible activation
 376 spaces requires and understanding of its internal density and
 377 not just its bounds. The density of **between-muscle** connec-
 378 tivity is seen directly by the density of the lines connecting
 379 the different muscles and cost functions. The **within-muscle**
 380 density can be computed by binning points at each activation
 381 level value.

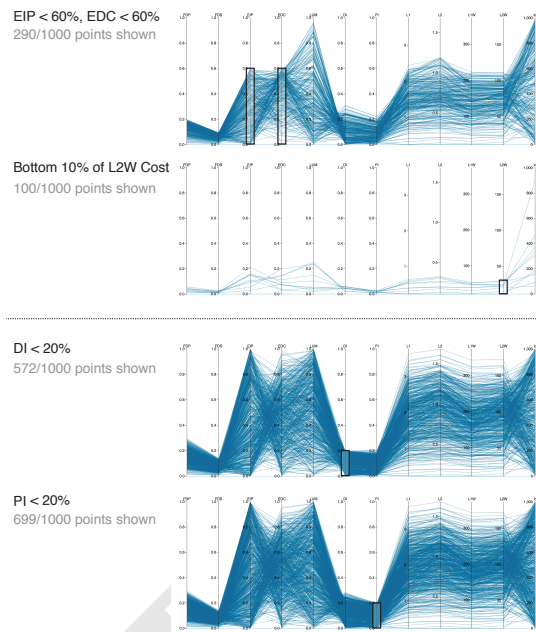
382 Lastly, those same connecting lines in the parallel coordi-
 383 nate visualization allow us to characterize the interrelatedness
 384 of valid solutions in 7-dimensional space. For example, the
 385 lines connecting FDP and FDS are mostly parallel, indicating
 386 a strong positive correlation. In fact, looking at these lines
 387 allows one to directly see and understand the Pearson product-
 388 moment correlation coefficients of 0.99, -0.50, and -0.06 in the
 389 adjacent muscle pairs FDP—FDS, LUM—DI, and EIP—EDC,
 390 respectively. The interactive parallel coordinate visualization
 391 also allows for any pairwise comparison by simply dragging
 392 and reordering the vertical axes—and hovering over individual
 393 data rows highlight an individual valid activation pattern atop
 394 all others.

395
 396 **Low-dimensional approximations to the feasible activation**
 397 **space.** We applied PCA (Principal Component Analysis) to
 398 the valid muscle activation patterns sampled uniformly at
 399 random from the feasible activation space. We show results for
 400 10 levels of task intensity. However, we did this in an iterative
 401 fashion to replicate the fact that experimental studies can only
 402 collect a finite amount of data from each subjects. Thus, from
 403 the total pool of 10,000 sub-sampled points sampled by Hit-
 404 and-Run (i.e., accepting every 100th point from 100,000 total
 405 samples to remove potential autocorrelation among points);
 406 sample sizes of 10, 100, and 1,000 points (i.e., simulated ‘ex-
 407 perimental’ sample sizes) were replicated 100 times each. We
 408 applied PCA to each set of sampled points.

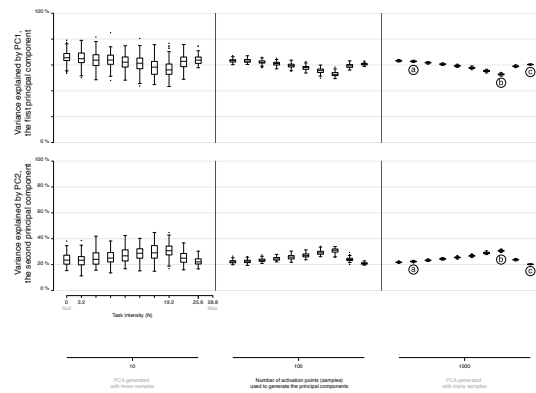
409 The variance explained by PC1 and PC2 (and its boxplot
 410 distribution) for all iterations are shown to change with task
 411 intensity for all sample sizes (Fig. 5). Explaining about 13–15%
 412 of the variance, PC3 is exactly equal to the remaining variance
 413 not explained by the first two components—this is a result of
 414 the feasible activation space being a 3-dimensional polytope
 415 P by construction (i.e., recall that 4 task constraints applied
 416 to 7 muscles produce a 3-dimensional polytope embedded in
 417 the 7-dimensional muscle activation space).

418 The boxplots in Fig. 5 quantify how different amounts of
 419 data change the estimates of variance explained by PC1 and
 420 PC2 with task intensity (c.f. labels a vs. b vs. c). We see
 421 this dispersion is small in the center and right columns. Note
 422 that the ratio of variance explained between PC1 and PC2
 423 between 50 to 80% of task intensity is indicative of changes in
 424 the aspect ratio of the feasible activation space—which we see
 425 changes with task intensity.

426 Importantly, using experimentally realistic samples sizes of
 427 10 repetitions per subject (leftmost column) not only does not
 428 capture this change, but its standard deviation is large enough
 429 to blur the statistically significant differences that are known
 430 to appear with larger (but experimentally unrealistic) sample
 431 sizes. The impact of impoverishing the number of samples fed
 432 to PCA reminds us that inadequate amounts of data obfuscate
 433 the underlying changes in the structure of the data analyzed
 434 (Fig. 5).



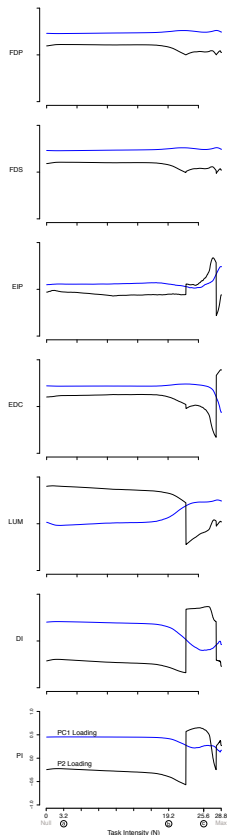
499
 500 **Fig. 4. Supplemental Figure: Posthoc constraints on a task intensity of 80%**
 501 Here we show four unique examples of constraints applied to the points collected
 502 from the feasible activation space. With this, we can rapidly predict how index finger
 503 control must change in the event of weakness in specific muscles. We also can see
 504 how many points remain once the constraints are added—signaling how the structure
 505 of the feasible force space is affected.



506
 507 **Fig. 5. Approximating the structure of feasible activation spaces via principal**
 508 **components analysis (PCA) is sensitive to both the number of points used and**
 509 **the intensity of the task.** Rows show the variance explained by the first (top) and
 510 second (bottom) principal components with increasing data points (left to right). It is
 511 not possible to generalize the variance explained across tasks intensities, and large
 512 numbers of points (i.e., > 100) are needed to confidently estimate the real changes
 513 in variance explained as a function of task intensity (cf. points labeled a, b, c).

497 There were also important changes in the loadings of the
 498 PC1 and PC2 vectors. While the ratio of variance explained
 499 between PC1 and PC2 gives a sense of the aspect ratio of
 500 the feasible activation space, the loadings of PC1 and PC2
 501 speak to its orientation. Fig. 6 shows how the loadings of
 502 the PC1 and PC2 vectors change across labels a, b, and c
 503 (Fig. 5) corresponding to 11, 66 and 88% of task intensity,
 504 respectively. What these loadings indicate are the direction in
 505 7-dimensional space, which changes dramatically.

506 These changes we see in (i) the lower and upper bounds of
 507 activations, and in (ii) the relative variance explained and (iii)
 508 loadings for PC1 and PC2, demonstrate that the size, shape
 509 and orientation of the feasible activation space changes with
 510 task intensity. Moreover, these changes represent the best-case
 511 scenario given the absence of experimental noise, within- and
 512 across-subject variability, and measurement error.



544 **Fig. 6. PCA loadings change dramatically as task intensity increases** For each
 545 of 1,000 task intensities, we collected 1,000 points from the feasible activation space,
 546 and computed three principal components. Note that the signs of the loadings depend
 547 on the numerics of the PCA algorithm, and are subject to arbitrary flips in sign—
 548 thus for clarity we plot them such that FDP's loadings in PC1 are positive at all
 549 task intensities. Synergies at representative task intensities a, b, c in Fig. 5 differ.
 550 This reflects changes in the geometric structure of the feasible activation space as
 551 redundancy is lost.

552 **Changes in the probabilistic structure of the feasible activation space with increasing task intensity, or how muscle redundancy is lost.** The maximal static fingertip force vector in
 553 a given direction is produced by a single and unique combi-
 554 nation of muscle activations. In contrast, any sub-maximal
 555 magnitude of that same vector is produced by an infinite num-
 556 ber of solutions (? ? ? ?). Our analysis of feasible activation
 557 spaces at different task intensities allows us to characterize how
 558 this redundancy changes and is lost. The histogram heatmaps
 559 in Fig. 7 illustrate the changes and shrinking of within-muscle
 560 density of valid activation levels for sub-maximal forces, con-
 561 verging to a single solution for maximal force output. These
 562 surface plots show how the normalized histograms (of 1,000
 563 valid activation levels for each muscle) change at each of 100
 564 levels of task intensity between 0 and 1. Following a muscle's
 565 column from bottom to top shows the activation histograms
 566 for each magnitude of distal force and ending, naturally, with
 567 a spike about the unique value at maximal force production.

568 The flat areas in each surface plot (e.g. clearly visible
 569 for DI) represent muscle activation levels that are not valid
 570 for that task intensity. That is, there exist no valid muscle
 571 activation patterns that contain that muscle at that level, and
 572 thus no points are found there.

573 These plots show the nature and rate of convergence to the
 574 unique solution for maximal force output across muscles. We
 575 find that the histograms of activation levels for each muscle
 576 need not be symmetric, nor have the same shape (skewness
 577 and kurtosis) as the magnitude of the output force increases.
 578 For some muscles the convergence accelerates after 60% or
 579 80% of task intensity (as in LUM and EIP), while others
 580 converge monotonically along the entire progression (e.g. DI
 581 and PI). The peaks (i.e. modes) of each histogram at each
 582 task intensity represents the slice of the polytope that has
 583 the largest relative volume along that muscle dimension (i.e.,
 584 greatest frequency of that level of muscle activation across all
 585 valid solutions). Importantly, for most muscles (FDP, FDS,
 586 EIP, EDC, and LUM), the mode is not necessarily located at
 587 the same relative level of activation needed for maximal force
 588 output. That is, the histogram at high levels of force is not
 589 simply a shifted version of the histogram at low levels of force.
 590 The histograms for DI are the exception, whose modes seems
 591 to scale linearly with task intensity.

592 These histograms, in conjunction with the results in the
 593 parallel coordinate visualization, also demonstrate that the
 594 structure of feasible activation spaces cannot be inferred from
 595 their bounding boxes alone (i.e., upper and lower activation
 596 bounds for each muscle). An immediate example is how,
 597 for most task intensities, both EIP and LUM have similar
 598 lower and upper bounds near 0 and 1, respectively—yet their
 599 distributions are thoroughly distinct.

Discussion

600 **Summary.** Feasibility theory, as a conceptual and computa-
 601 tional approach, is a means to pierce the curse of dimensionality
 602 to establish a physics-based ground truth for neuromuscular
 603 control. This practical approach can now characterize—in a
 604 complete way—the set of all valid ways to activate multiple
 605 muscles to produce a given task. Feasible activation spaces
 606 are, in fact, *the* neuromechanical landscapes upon which all
 607 neuromuscular learning, control, and performance must occur.
 608 Therefore, we provide an integrative and unifying perspective
 609 that demonstrates how today's dominant theories of neuromuscular
 610 control are alternative approximations to feasible
 611 activation spaces from optimization, geometric, and proba-
 612 bilistic perspectives.

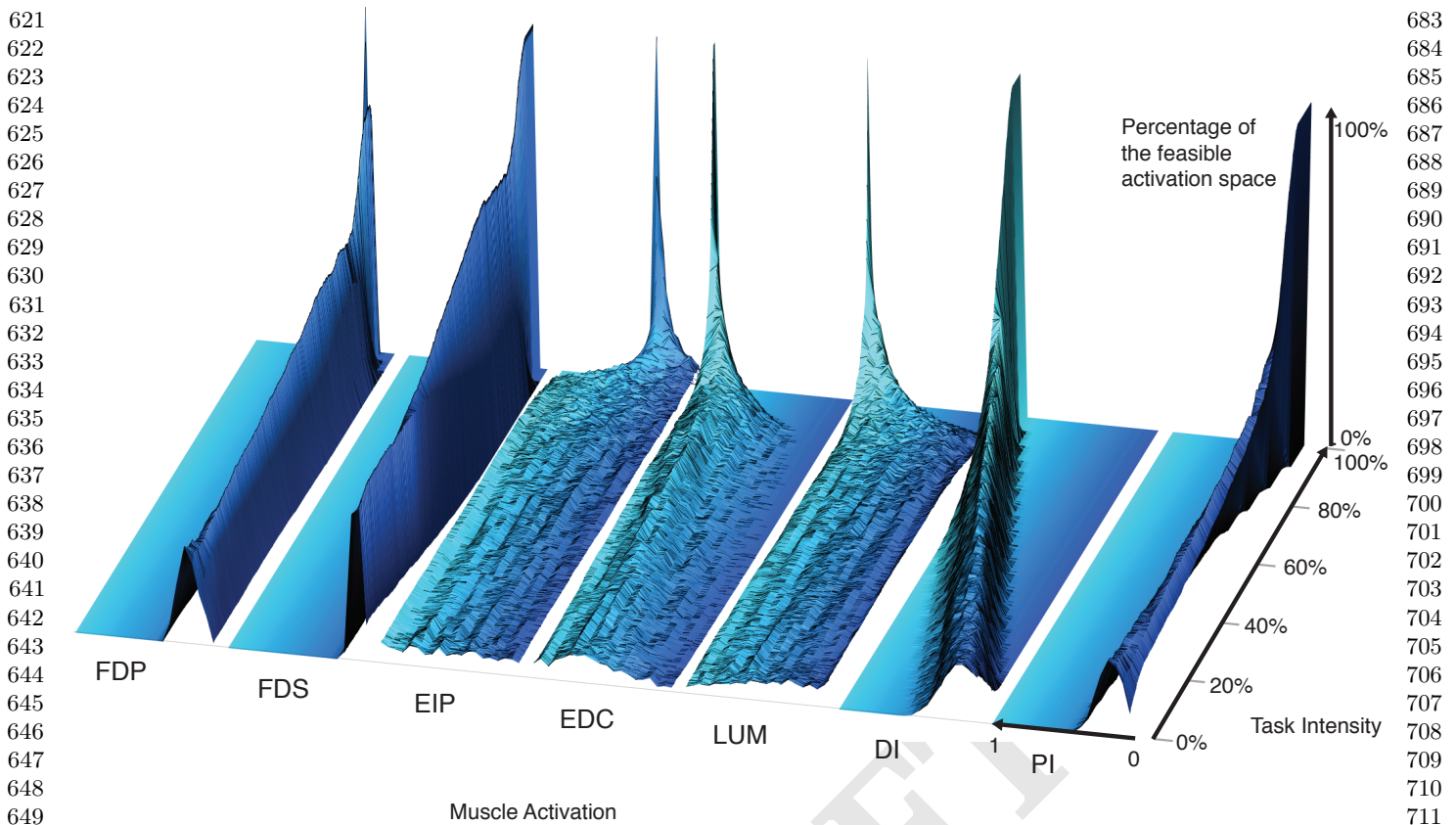


Fig. 7. The within-muscle probabilistic structure of feasible muscle patterns across 1,000 levels of fingertip task intensity. The changes in the breadth and height for each muscle reveal muscle-specific consequences of task intensity on their probability distributions. The cross-section of each density plot is the 50-bin histogram of activation for each muscle, at that task intensity. Height represents the percentage of solutions for that task. The axis going into the page indicates increasing fingertip task intensity up to 100% of maximal. Color is used to provide perspective.

The value of a cost function. Optimization is the oldest computational approach to finding valid muscle activation patterns that produce limb function (e.g., (?)). While optimization is a reasonable hypotheses to explore neuromuscular control (?), some criticize it as mathematical abstraction that anthropomorphizes neurons with the ability to choose, evaluate and follow cost functions in high-dimensions (? ?). There is an intimate relationship between optimization and feasible activation spaces (?). Optimization is analogous to finding a best solution in the dark—guided by repeated evaluations of a cost-function. Computing the feasible activation space is then a means to ‘turn on the lights’ to see all possible valid solutions independently of cost (?). Our complete sampling of high-dimensional feasible activation spaces (? ?) allows us to compare and contrast *families* of solutions instead of *individual* optimal solutions for a particular cost function. Fig. 3 demonstrates a complete description of families of valid coordination patterns and their relationship to alternative costs. Importantly, similar valid muscle activation patterns can have dissimilar costs, and vice versa.

Because these explorations can be done for alternative cost functions, they can provide quantitative overall descriptions of high-dimensional ‘cost landscapes.’ By not having to insist on (or settle for) individual optimal—or near-optimal—solutions, we now have the same ability the nervous system has to explore, compare and contrast multiple valid ways to coordinate

muscles. Importantly, the relationships among valid muscle activation patterns emerge naturally from the physical properties of the limb and definition of the task. This cost-agnostic approach allows us to re-evaluate our assumptions about what the nervous system cares—and does not care—about. Lastly, this cost-agnostic approach also provides a powerful tool for inverse optimization, i.e., uncovering latent cost functions from data (?). Our comparison across cost functions using parallel coordinates is already a form of inverse optimization.

Structure, correlation, and synergies. The physical properties of the limb and definition of the task also define a low-dimensional structure of the feasible activation space (?). Therefore, it is expected that experimental recordings of muscle activations during limb function will exhibit a dimensionality that is smaller than the number of muscles (? ?). Thus, applying PCA to the points sampled from the feasible activation space also finds that few PCs can explain the variance in the data.

This application of PCA at increasing task intensities (i.e., as muscle redundancy is lost) allows us to demonstrate—for the first time to our knowledge—several important features and limitations of dimensionality reduction. For example, we see that the aspect ratio (Fig. 5) and orientation (Fig. 6) of the feasible activation spaces change as their size shrinks (Fig. 7). Thus, such *descriptive* synergies extracted from limited experimental observations likely do not generalize well across task

745 intensities. It is important to distinguish *descriptive* synergies
746 (the dominant approach in the literature to extract synergies
747 from experimental data using dimensionality reduction tech-
748 niques such as PCA) from *prescriptive* synergies (those known
749 to be implemented by the controller) (?).

750 This also has important consequences to motor control and
751 learning. Producing force vectors at the endpoint of a finger
752 or limb with accurate magnitude and direction are critical
753 for versatile manipulation and locomotion (? ? ?). If a
754 given synergy can produce such accurate force vectors only
755 for a given task intensity (and thus inaccurate ones at other
756 intensities), then the attractiveness of synergies to simplify the
757 neuromuscular control of the limb is reduced. To compensate,
758 the nervous system would need to learn, recall and implement
759 specific synergies for each force level. In prior experimental
760 work, we have shown that the nervous system produces accu-
761 rate fingertip forces of different magnitudes by, instead, likely
762 scaling a remembered muscle activation pattern to produce
763 forces of different magnitudes, together with a full-dimensional,
764 real-time error correction neural controller (?). Note that
765 interpreting this experimental result still as a synergy-based
766 approach would defeat the purpose of synergies as a means to
767 simplify the control by reducing its dimensionality.

768 Our results also show how experiments with realistically
769 moderate numbers of participants and test trials likely do
770 not contain sufficient data to produce robust estimates of de-
771 scriptive synergies across task intensities. As per the curse
772 of dimensionality, sampling uniformly at random from high-
773 dimensional spaces is exponentially difficult. Thus, even for
774 this anatomically complete 7-muscle finger model, PCA de-
775 pends strongly on the number of independent observations,
776 such as uncorrelated trials from one subject or different sub-
777 jects. Figure 5 shows that 100 to 1,000 such ideal data points
778 from a simulated ‘test subject’ are needed to produce accurate
779 estimates of changes in PC1 and PC2 with task intensity (c.f.
780 labels a vs. b vs. c). Future studies should explore how many
781 experimental data points are sufficient from a given subject
782 when recording from only a subset of the many (20+) muscles
783 of human limbs in the presence of experimental noise, inherent
784 stochasticity of EMG, and within- and between-subject vari-
785 ability. Some studies have begun to ask subjects to explore
786 different ways to perform a given task (?) (i.e., estimate
787 the structure of the feasible activation space), but in practice
788 such studies cannot likely collect sufficient data uniformly
789 at random to obtain accurate estimates of the descriptive
790 synergies (?). While our results suggest caution when in-
791 terpreting synergies obtained experimentally, we underscore
792 that dimensionality-reduction is a useful approach to capture
793 global geometric properties of feasible activation spaces.

794 **Toward probabilistic neuromuscular control.** Our results are
795 particularly empowering for the emerging field of probabilistic
796 neuromuscular control (? ? ? ?). Suppose that the nervous
797 system uses some form of probabilistic or Bayesian learning
798 and control strategy. Such approach requires two enabling—
799 and biologically feasible—elements: *trial-and-error iterative*
800 *exploration*, and *memory-based exploitation* of the probability
801 density functions used to approximate the feasible activation
802 spaces (?). The parallel coordinate plots and histograms in
803 Fig. 2 and 7 provide, to our knowledge, the first complete (?
804 ?) characterization of such multi-dimensional joint proba-
805 bility density functions for a realistic tendon-driven system

807 performing a well-defined task.

808 These techniques and results now empower the study of
809 fundamental aspects of probabilistic control. For example, an
810 organism can only execute so many trial-and-error iterations
811 during learning, likely too few to completely and exhaustively
812 sample the high-dimensional feasible space of interest. This
813 makes it much more likely that, by virtue of being more easily
814 found, an organism will find and preferentially exploit the
815 strong modes (i.e., narrow and high peaks in Figs. 3, 4, and
816 7) of the multi-dimensional probability density functions than
817 any other region of feasible activation spaces. Thus, first,
818 the maximal ranges of feasible activations described by the
819 bounding box (? ?) may have little practical bearing on how
820 those tasks are learned and executed. And second, those same
821 strong modes would represent strong attractors to create and
822 reinforce motor habits. Habitual control has been proposed
823 based on experimental and empirical data as an alternative
824 to a strict optimization approach to neuromuscular control (?).
825 Our work now provides the computational means to link
826 habitual to probabilistic control. This allows us to generate
827 testable hypotheses of how these motor habits are defined by
828 the structure of the feasible activation space, how they are
829 learned by the organism, and how difficult or easy it is to
830 break out of them.

831 Thus, motor learning likely needs to proceed from adopting
832 easily-found solutions independently of their cost, to using
833 some low dimensional approximation to the gradient of the cost
834 landscape, to then transitioning to less likely but potentially
835 less costly subregions of the solutions space. This integrative
836 perspective leads us to propose a hybrid approach to motor
837 learning and execution where the practical limits on trial-and-
838 error iterations are coupled with the low-dimensional structure
839 of the solution space to enable some form of heuristic local
840 optimization to create sub-optimal motor habits. Importantly,
841 the organism performs strict optimization or synergy control at
842 its peril. Take, for example, the case of a 2-dimensional feasible
843 activation space embedded in 3-D, Fig. 8e. Taking a step from
844 any one valid point to another valid point on the plane runs the
845 risk of ‘falling off’ the solution space and failing at the task—a
846 risk that is exponentially exacerbated in higher-dimensions.
847 Thus, improvements in the neighborhood of a good solution
848 necessarily risk task failure and potential injury. These are all
849 arguments in support of the evolutionary and developmentally
850 useful strategy to use good-enough control based on habit or
851 sensorimotor memory rather than optimization (? ?). This
852 may explain why mass practice and coaches are so critical to
853 achieve elite athletic performance (?).

854 **Clinical implications.** This line of thinking has consequences
855 to neurorehabilitation. Neurological conditions disrupt feasi-
856 ble activation spaces, be it by affecting anatomy of the limb,
857 muscle strength and independence with which muscles can be
858 controlled. Functional recovery following the disruption, if
859 not destruction, of the landscape of valid muscle activation
860 patterns requires re-learning existent, or building new, proba-
861 bility density functions. This occurs just when older adults
862 suffer from reduced perceptuo-motor learning rates (?).

863 A probabilistic landscape for neuromuscular function begins
864 to explain why neurorehabilitation in aging adults is so difficult
865 (e.g., (?)) and why motor learning in children takes thousands
866 of repetitions (?)—while also generating new rehabilitation
867 strategies, and testable hypotheses around them, that leverage
868

869	knowledge of the nature and structure of feasible activation	931
870	spaces.	932
871		933
872	Author Affiliations. Include department, institution, and	934
873	complete address, with the ZIP/postal code, for each author. Use	935
874	lower case letters to match authors with institutions, as shown	936
875	in the example. Authors with an ORCID ID may supply this	937
876	information at submission.	938
877		939
878	Submitting Manuscripts. All authors must submit their arti-	940
879	cles at PNAScentral . If you are using Overleaf to write your	941
880	article, you can use the “Submit to PNAS” option in the top	942
881	bar of the editor window.	
882		
883	Format. Many authors find it useful to organize their	943
884	manuscripts with the following order of sections; Title, Author	944
885	Affiliation, Keywords, Abstract, Significance Statement, Re-	945
886	sults, Discussion, Materials and methods, Acknowledgments,	946
887	and References. Other orders and headings are permitted.	947
888		948
889	Manuscript Length. PNAS generally uses a two-column	949
890	format averaging 67 characters, including spaces, per line. The	
891	maximum length of a Direct Submission research article is six	
892	pages and a PNAS PLUS research article is ten pages includ-	
893	ing all text, spaces, and the number of characters displaced	
894	by figures, tables, and equations. When submitting tables,	
895	figures, and/or equations in addition to text, keep the text for	
896	your manuscript under 39,000 characters (including spaces) for	
897	Direct Submissions and 72,000 characters (including spaces)	
898	for PNAS PLUS.	
899		
900	References. References should be cited in numerical order	950
901	as they appear in text; this will be done automatically via	951
902	bibtex, e.g. (?) and (??). All references, including	952
903	for the SI, should be included in the main manuscript file.	953
904	References appearing in both sections should not be duplicated.	954
905	SI references included in tables should be included with the	955
906	main reference section.	956
907		957
908	Data Archival. PNAS must be able to archive the data essential	958
909	to a published article. Where such archiving is not possible,	959
910		
911		
912	$\begin{aligned}(x+y)^3 &= (x+y)(x+y)^2 \\ &= (x+y)(x^2 + 2xy + y^2) \\ &= x^3 + 3x^2y + 3xy^2 + y^3.\end{aligned}$	[1] 960
913		961
914		962
915		963
916		964
917		965
918		966
919		967
920	Supporting Information (SI). The main text of the paper must	968
921	stand on its own without the SI. Refer to SI in the manuscript	969
922	at an appropriate point in the text. Number supporting figures	970
923	and tables starting with S1, S2, etc. Authors are limited to	971
924	no more than 10 SI files, not including movie files. Authors	972
925	who place detailed materials and methods in SI must provide	973
926	sufficient detail in the main text methods to enable a reader	974
927	to follow the logic of the procedures and results and also must	975
928	reference the online methods. If a paper is fundamentally a	976
929	study of a new method or technique, then the methods must	977
930	be described completely in the main text. Because PNAS edits	978
931		979
932		980
933		981
934		982
935	Table 1. Comparison of the fitted potential energy surfaces and ab	983
936	initio benchmark electronic energy calculations	984
937		
938		
939		
940		
941		
942		
943		
944		
945		
946		
947		
948		
949		
950		
951		
952		
953		
954		
955		
956		
957		
958		
959		
960		
961		
962		
963		
964		
965		
966		
967		
968		
969		
970		
971		
972		
973		
974		
975		
976		
977		
978		
979		
980		
981		
982		
983		
984		
985		
986		
987		
988		
989		
990		
991		
992		

nomenclature for the TSs refers to the numbered species in the table.

- 993 SI and composes it into a single PDF, authors must provide
 994 the following file formats only.
 995
- 996 **SI Text.** Supply Word, RTF, or LaTeX files (LaTeX files must
 997 be accompanied by a PDF with the same file name for visual
 998 reference).
- 999 **SI Figures.** Provide a brief legend for each supporting figure
 1000 after the supporting text. Provide figure images in TIFF, EPS,
 1001 high-resolution PDF, JPEG, or GIF format; figures may not
 1002 be embedded in manuscript text. When saving TIFF files, use
 1003 only LZW compression; do not use JPEG compression. Do
 1004 not save figure numbers, legends, or author names as part of
 1005 the image. Composite figures must be pre-assembled.
 1006
- 1007 **3D Figures.** Supply a composable U3D or PRC file so that it
 1008 may be edited and composed. Authors may submit a PDF file
 1009 but please note it will be published in raw format and will not
 1010 be edited or composed.
 1011
- 1012 **SI Tables.** Supply Word, RTF, or LaTeX files (LaTeX files must
 1013 be accompanied by a PDF with the same file name for visual
 1014 reference); include only one table per file. Do not use tabs or
 1015 spaces to separate columns in Word tables.
 1016
- 1017 **SI Datasets.** Supply Excel (.xls), RTF, or PDF files. This file
 1018 type will be published in raw format and will not be edited or
 1019 composed.
 1020
- 1021 **SI Movies.** Supply Audio Video Interleave (avi), Quicktime
 1022 (mov), Windows Media (wmv), animated GIF (gif), or MPEG
 1023 files and submit a brief legend for each movie in a Word or
 1024 RTF file. All movies should be submitted at the desired re-
 1025 production size and length. Movies should be no more than
 10 MB in size.
 1026
- 1027 **Still images.** Authors must provide a still image from each video
 1028 file. Supply TIFF, EPS, high-resolution PDF, JPEG, or GIF
 1029 files.
 1030
- 1031 **Appendices.** PNAS prefers that authors submit individual
 1032 source files to ensure readability. If this is not possible, supply
 1033 a single PDF file that contains all of the SI associated with
 1034 the paper. This file type will be published in raw format and
 1035 will not be edited or composed.
 1036
- 1037 **Materials and Methods**
- 1038 The methods to obtain feasible activation spaces for ‘tendon-driven’,
 1039 limbs are described in detail in the textbook *Fundamentals of
 1040 Neuromechanics* and references therein (?). This tendon-driven
 1041 approach explicitly and distinctly avoids the conceptual approach
 1042 to combine multiple muscle actions into net torques at each joint.
 1043 Rather, it emphasizes studying the individual actions of all muscles
 1044 at all levels of analysis, from their neural activation to their
 1045 contributions to fingertip force. We describe them briefly here.
 1046
- 1047 **Theory.** As described in (?), consider a tendon-driven limb, such as
 1048 a finger, with n independently controllable muscles, where we define
 1049 the neural command to each muscle as a positive value of activation
 1050 between 0 (no activation) and 1 (maximal activation). We can then
 1051 visualize the set of all feasible neural commands (i.e., all possible
 1052 muscle activation patterns) as the points contained in a positive
 1053 n -dimensional cube with sides of length equal to 1. A specific muscle
 1054 activation pattern is a *point* (i.e., an n -dimensional vector \mathbf{a}) in this
 n-dimensional cube (? ? ? ?). Now consider a specific task, such
 as producing a vector of static force with the fingertip, as when
 holding an object. Clearly, not all muscle activation patterns inside

the n -dimensional cube can produce that desired static fingertip force vector: The lengths of the bones, the number and type of kinematic degrees of freedom, the anatomical routing of the tendons of each muscle, the posture of the finger, and the relative strengths of the muscles define which subset of points in the n -cube can produce a fingertip force vector of a specific magnitude and direction. As described in (? ? ?) the musculoskeletal anatomy of the limb, the need to control individual tendons, and the physics of a motor task uniquely specify a polytope embedded in \mathbb{R}^n (i.e., the feasible activation space). This polytope contains the family of (potentially infinite) valid muscle activation patterns that can produce this static force production task. However, these valid muscle coordination patterns are not arbitrarily different because, by construction, the geometric structure of the polytope that contains them defines strict spatial correlations among them (?).

System of linear equations to simulate static force production by a tendon-driven system Consider producing a vector of static force with the endpoint of the limb in a given posture. The constraints that define that task (i.e., the direction and magnitude of the force vector at the endpoint) are linear equations (?) that come from the mapping between neural activation of individual muscles to static endpoint forces and torques the limb can produce. This mapping is linearly modeled by the equation

$$\begin{pmatrix} f_x \\ f_y \\ f_z \\ \tau_x \\ \tau_y \\ \tau_z \end{pmatrix} = \mathbf{w} = H\mathbf{a} = H \begin{pmatrix} a_1 \\ a_2 \\ a_3 \\ \dots \\ a_n \end{pmatrix}, \mathbf{a} \in [0, 1]^n \quad [2]$$

where H is the matrix of linear constraints defined by the musculoskeletal anatomy of the limb (?), \mathbf{a} is the input vector of n muscle activations, $\mathbf{f} \in \mathbb{R}^m$ is the m -dimensional limb output ‘wrench’ (i.e., the forces and torques the finger can produce at the endpoint).

The output wrench, m , is at most 6-dimensional (i.e., 3 forces and 3 torques) depending on the number of kinematic degrees of freedom of the limb, and usually $m < n$ because limbs have more muscles than kinematic degrees of freedom (?). Muscles can only pull, so elements of \mathbf{a} cannot be negative, and are capped at 1 (i.e., 100% of maximal muscle activation).

What are the muscle coordination patterns that produce a given task? As explained in (?), the task of producing a static fingertip force vector is defined by specifying the desired values for the elements of the endpoint forces and torques of \mathbf{w} . Each such constraint equation defines a hyperplane of dimension $n-1$, and their combination defines the task completely. The *feasible activation space* of the task, if it is well posed (?), is defined by the points \mathbf{a} that lie within the n -cube and at the intersection of all constraint hyperplanes.

Geometrically speaking, the feasible activation space is a $(n-m)$ -dimensional convex polytope P embedded in \mathbb{R}^n that contains all n -dimensional muscle coordination patterns (i.e., points \mathbf{a}) that satisfy all constraints, and therefore can produce the task. Increasing task specificity by adding more constraints naturally decreases the dimensionality and changes the size and shape of the feasible activation space (? ? ?).

The Hit-and-Run algorithm uniformly samples from feasible activation spaces The goal is to characterize the qualities that define all valid muscle activation patterns (i.e., n -dimensional vectors \mathbf{a}), that are points that make up P . This is equivalent to characterizing the structure of the convex polytope P . But calculating the geometric properties of convex polytopes in high dimensions is computationally challenging. Taking the generalized concept of an n -dimensional volume as an example of a geometric property of interest, the exact volume computations for n -dimensional polytopes is known to be tractable only in a polynomial amount of time (i.e., $\#P$ -hard) (?). Currently available volume algorithms can only handle polytopes embedded in small dimensions like 10 or slightly more (?). Studying vertebrate limbs in general, however, can require including several dozen muscles, such as our studies of a 17-muscle human arm and a 31-muscle cat hindlimb model (?); and other limb models have over 40 muscles such as (? ? ? ?).

Similar difficulties arise when computing other geometric properties such as the shape and aspect ratio of P in high dimensions. We

and others have described polytopes P by their bounding box (i.e., the range of values in every dimension) (? ?), but that singularly overestimates the shape and volume of the feasible activation space as discussed in (?). Take Fig. 8e as an example, where the bounding box of the 2-dimensional polygon has a volume—even though a plane has zero volume—, and can be almost as large as the positive unit cube itself. Similar problems arise in the interpretation of the inscribed and circumscribed ball (?).

We propose a complete probabilistic method to describe the structure of feasible activation spaces P . This includes the descriptive statistics, histograms, and point densities of the set of valid muscle activation patterns \mathbf{a} uniformly sampled from the polytope. To do so, we use the Hit-and-Run method. Experimentally, it is known to converge to a uniform sampling across any convex body, up to about 40 dimensions (?). The Hit-and-Run method is a generalization of a discrete Markov chain—where the goal is to identify multiple points from the feasible activation polytope P uniformly-at-random.

The Hit-and-Run algorithm is defined as follows (it works analogously for any convex body even if not a polytope)(?):

1. Find a point \mathbf{p} in P to use as a starting point by using the linear programming method documented in the Supplementary Note.
2. Generate a line in a random direction q (uniformly-at-random over all directions) from \mathbf{p} in P (Fig. 8a).
3. Find the two intersection points of the line given by the random direction q with the boundary of the polytope (Fig. 8b).
4. Choose a new point uniformly-at-random on the line segment between the intersection points (Fig. 8c).
5. Repeat the above steps from 2. onwards using the new point as the starting point, and generate a new random direction. Continue this process for s iterations, where s is the mixing number. The mixing number is the number of iterations that are expected to result in a point sampled uniformly at random from the space, with respect to the starting point (and any other point in P). Saving just the s^{th} point for many repetitions will result in many uniform-at-random points collected across the feasible activation space (Fig. 8).

We describe the mathematical basis and details to replicate our implementation in the Supplementary Note, including our application of slack variables to select a valid starting point within the feasible activation space.

Example of a tendon-driven system.

Realistic 3-D model of a 7-muscle human index finger We applied this methodology to our published model of an index finger for static fingertip force production. The model is described in detail elsewhere (?). Briefly, the input to the model is a 7-D muscle activation pattern \mathbf{a} , and the output is a 4-D wrench (i.e., static forces and torque) at the fingertip \mathbf{w}

$$\mathbf{w} = \mathbf{H}\mathbf{a} \quad [3]$$

$$\mathbf{H} = \mathbf{J}^{-T} \mathbf{R} \mathbf{F}_o \quad [4]$$

$$\mathbf{H} \in \mathbb{R}^{4 \times 7} \quad [5]$$

where

$$\mathbf{a} = \begin{pmatrix} a_{FDP} \\ a_{FDS} \\ a_{EIP} \\ a_{EDC} \\ a_{LUM} \\ a_{DI} \\ a_{PI} \end{pmatrix} \quad [6]$$

In Cartesian coordinates, the output wrench is

$$\mathbf{w} = \begin{pmatrix} f_x \\ f_y \\ f_z \\ \tau_x \end{pmatrix} \quad [7]$$

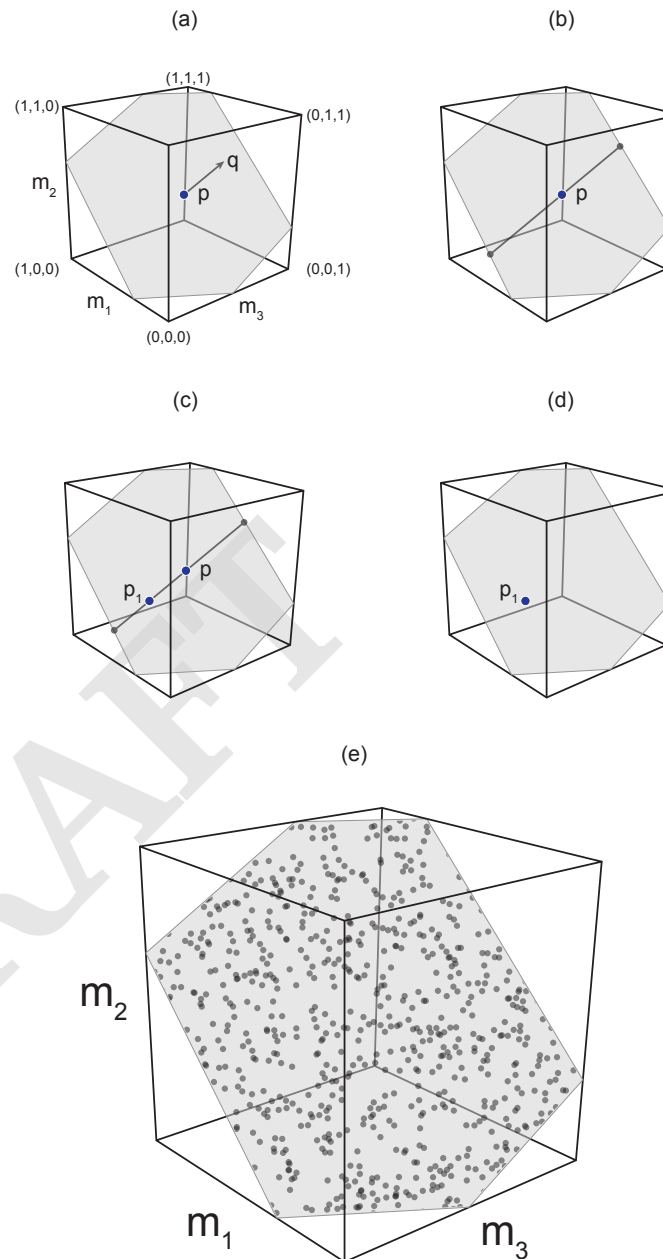


Fig. 8. Characterizing the high-dimensional structure of a feasible activation set via the Hit-and-Run algorithm (?). For a large class of biomechanical tasks, the feasible activation set is a convex polytope. Here we show a 3-muscle system as a schematic example upon which Hit-and-Run can be applied. We select a valid direction at random (a), and project a line to both boundaries (b). After selecting a point at random from the resulting line (c), we get a new valid point p_1 (d). Repeating steps a-d many (e.g., 100,000) times, and down-sampling those points, produces a statistically complete representation of the polytope (e)—and of the high-dimensional structure of the feasible activation set.

1241 which corresponds to these anatomical directions shown in
 1242 Fig. 1e.

$$w = \begin{pmatrix} f_{radial} \\ f_{distal} \\ f_{palmar} \\ \tau_{radial} \end{pmatrix} \quad [8]$$

1243 The biomechanical model H includes three serial links articulated by four kinematic degrees of freedom (ad-abduction, flexion-extension at the metacarpophalangeal joint, and flexion-extension at the proximal and distal interphalangeal joints). The action of each of the seven muscles (FDP: *flexor digitorum profundus*, FDS: *flexor digitorum superficialis*, EIP: *extensor indicis proprius*, EDC: *extensor digitorum communis*, LUM: *lumbrical*, DI: *dorsal interosseous*, and PI: *palmar interosseous*) on each joint to produce torque is given by the moment arm matrix $R \in \mathbb{R}^{4 \times 7}$. Lastly, $J \in \mathbb{R}^{4 \times 4}$ and $F_0 \in \mathbb{R}^{7 \times 7}$ are the Jacobian of the fingertip with 4 kinematic degrees of freedom, and the diagonal matrix containing the maximal strengths of the seven muscles, respectively (??). The finger posture was defined to be 0° ad-abduction and 45° flexion at the metacarpophalangeal joint, and 45° and 10° flexion, respectively, at the proximal and distal interphalangeal joints.

1244 **Feasible activation space for a static fingertip force task** Our goal
 1245 is to find the family of all feasible muscle activation patterns that
 1246 can produce a given task. In particular, the task we explored is
 1247 producing various magnitudes of a submaximal static force in the
 1248 distal direction f_{distal} — in the absence of any τ_{radial} , shown in
 1249 Fig. 1f. Therefore the feasible activation space is a polytope P in
 1250 7-dimensional activation space that meets the following four linear
 1251 constraints in a (??).

$$f_{radial} = 0 \quad [9]$$

$$f_{distal} = \text{desired magnitude as \% of maximal} \quad [10]$$

$$f_{palmar} = 0 \quad [11]$$

$$\tau_{palmar} = 0 \quad [12]$$

1252 These four constraints on the static output of the finger yield a 3-dimensional (i.e., $7 - 4 = 3$) polytope P embedded in 7-dimensional activation space. For details on how to create such models, apply 1253 task constraints and find such polytopes via vertex enumeration methods, see (??).

1254 Thus all valid output wrenches will have the form

$$w = \begin{pmatrix} 0 \\ \text{Desired distal task intensity in N} \\ 0 \\ 0 \end{pmatrix} \quad [13]$$

1255 For the index finger model used in this paper, the published
 1256 maximal feasible force in the distal direction is 28.81 Newtons. We
 1257 defined the normalized desired distal task intensity as a value ranging
 1258 between 0 and 1, i.e., each submaximal force can be produced by
 1259 any of the points contained in its corresponding feasible activation
 1260 space. For the production of a maximal force with $\alpha = 1$ the feasible
 1261 activation space shrinks to a single point (??).

1262 **Analysis of feasible activation spaces.**

1263 **Parallel coordinates visualization shows the location of all points
 1264 across all dimensions** Parallel coordinates are a common graphical approach to visualize interactions among high-dimensional data, which has been used in biomechanical studies (??). To demonstrate this visualization method, consider the results of the simple 3-dimensional example shown in Fig. 8e. We begin by drawing n parallel vertical lines for each of the dimensions n (i.e., 3 muscles). With the axis limits of each line set between 0 and 1, each point (Fig. 2a) is then represented by connecting their coordinates by $n - 1$ lines as shown in Fig. 2b.

1265 **Neural and metabolic cost functions** As mentioned in the Introduction, the field of neuromuscular control has a long historical tradition of using optimization to find muscle activation patterns that minimize effort, which requires the (often contentious) definition of cost functions (??). Therefore, we used four representative cost functions to calculate the relative fitness of each of the muscle activation patterns sampled—in effect also calculating

1266 the fitness landscape across all possible solutions. The cost functions are defined at the level of neural effort (L_1 , and L_2 norms); and at the level of metabolic cost, thought to be approximated by neural drive weighted by the strength of each muscle (L_1^w and L_2^w norms) (??).

1267 To visualize the costs associated with each valid muscle coordination pattern, we simply added four vertical lines at the far right of the parallel coordinates plot, one for each cost function, Fig. 2c. The variables a_i and F_{0i} represent the activation of the i^{th} muscle in a given muscle activation pattern, and the maximal strength of each muscle (??). Maximal muscle strengths are approximated by multiplying each muscle's physiological cross-sectional area, in cm^2 , by the maximal active muscle stress of mammalian muscle, 35 N/cm^2 (??). These four cost functions are but four examples as the literature contains many others as any investigator is in fact free to chose any cost function deemed relevant to their study.

1268 **Histograms of the activation level of each muscle across all valid solutions** Muscle-by-muscle histograms are another straightforward way to visualize the many points sampled from the convex polytope. Histograms are particularly helpful because they are approximations to probability density functions. They visualize the relative number of solutions (i.e., density of solutions) that required a particular level of activation from a particular muscle within its range of [0, 1]. In addition, the upper and lower bounds of the histograms show, in fact, the size of the side of the bounding box of the polytope in every dimension (i.e., for independently controlled muscle).

1269 **Dimensionality reduction** Investigators have repeatedly reported that electromyographical signals (i.e., experimental estimates of muscle activation patterns) tend to exhibit strong correlations with one another. In these experimental descriptions of dimensionality reduction of neuromuscular control, only few independent functions—sometimes called synergies—suffice to explain the majority of the variability in the observed muscle activation patterns (??). Principal components analysis (PCA) is a widely used technique to extract these few independent basis functions (correlation vectors called principal components, PCs) from high-dimensional data (??). In this case, PCs are often called the experimental representations of synergies of neural origin (??).

1270 Therefore, we also applied PCA to points (i.e., muscle coordination patterns) sampled from the feasible activation space at each force level. This provides the PCs that describe the correlations among valid muscle activation patterns for a given task. For example, the feasible activation space P in Fig. 8e is a 2-dimensional polygon embedded in 3-dimensional activation space. Thus, applying PCA to points sampled from the polygon will extract 2 synergies (i.e., 3-dimensional correlation vectors PC1 and PC2) that wholly explain the feasible activation space. By extension, in the case of fingertip force production in Fig. 1, the feasible activation space is a 3-dimensional polytope embedded of the 7-dimensional activation space. And PCA should extract, by construction, as many synergies as there are dimensions in the feasible activation space. For static force production with the index fingertip (i.e., 7 muscles and 4 constraints), we know that 3 principal components should describe 100% of the variance in points sampled from the feasible activation space (i.e., 7-dimensional correlation vectors PC1, PC2, and PC3).

1271 Applying PCA to our data allows us to test whether and how its results change when applied to feasible activation spaces for different magnitudes of fingertip force. We applied PCA to feasible activation spaces for fingertip task intensities ranging from 0 to 90% of maximal. We compare both the variance explained by each PC and their vector direction (i.e., the ‘loadings’ or correlations among muscle (??)) as the force level increases. Lastly, we tested whether our PCA results are sensitive to the number of points sampled from each feasible activation space. This is important because experimental studies test 10 or so subjects in practice, which may be too few when sampling from high-dimensional spaces.

1272 **ACKNOWLEDGMENTS.** Research reported in this publication
 1273 was supported by the National Institute of Arthritis and Musculoskeletal and Skin Diseases of the National Institutes of Health (NIH) under Awards Number R01 AR-050520 and R01 AR-052345 to FVC, and the Swiss National Science Foundation (SNF Project 1274 200021_150055 / 1) to BG, KF and FVC. The content is solely the
 1275